Research Article

Abdur Rahman Shaukat, Peng Lan*, Jia Wang, Tengfei Wang, and Nianli Lu

In-plane nonlinear postbuckling and buckling analysis of Lee's frame using absolute nodal coordinate formulation

https://doi.org/10.1515/cls-2022-0212
received November 14, 2022; accepted July 15, 2023

Abstract: In this study, four absolute nodal coordinate formulation (ANCF)-based approaches are utilized in order to predict the buckling load of Lee's frame under concentrated load. The first approach employs the standard two-dimensional shear deformable ANCF beam element based on the general continuum mechanics (GCM). The second approach adopts the standard ANCF beam element modified by the locking alleviation technique known as the strain-split method. The third approach has the standard ANCF beam element with strain energy modified by the enhanced continuum mechanics formulation. The fourth approach utilizes the higher-order ANCF beam element based on the GCM. Two buckling load estimation methods are used, *i.e.*, by tracing the nonlinear equilibrium path of the load–displacement space using the arc-length method and applying the energy criterion, which requires tracking eigenvalues through the dichotomy scheme. Lee's frame with different boundary conditions including pinned–pinned, fixed-pinned, pinned-fixed, and fixed–fixed are studied. The complex nonlinear responses in the form of snap-through, snap-back, and looping phenomena during nonlinear postbuckling analysis are simulated. The critical buckling loads and buckling mode shapes obtained through the energy criterion-based buckling method are obtained. After the comparison, higher-order beam element is found to be more accurate, stable, and consistent among the studied approaches.

Keywords: absolute nodal coordinate formulation, buckling analysis, nonlinear postbuckling analysis, arc-length method, Lee's frame

1 Introduction

Absolute nodal coordinate formulation (ANCF) is a nonincremental nonlinear finite-element formulation originally proposed for the dynamics analysis of large-deformation and large-rotation multibody systems by Shabana [1]. ANCF utilizes the global nodal position and gradients as degrees of freedom (DOFs). Consequently, the formulation leads to a constant mass matrix in the equations of motion and further leads to zero centrifugal and Coriolis forces [2]. Additionally, it imposes no restrictions on the amount of rotation or deformation within the ANCF element and is consistent with the theory of nonlinear general continuum mechanics (GCM) [3]. Due to the above merits, ANCF has been applied in the nonlinear dynamics analysis of vehicle chassis with leaf spring systems [4–6], space structures [7–9], and soft robotics [3,10–12]. In addition, the capabilities of ANCF in the nonlinear static analysis have also been verified by some benchmark problems [13,14]. Therefore, ANCF which was originally proposed to study nonlinear dynamics is useful in the nonlinear static analysis while new elements are regularly being introduced [15].

Compared with the existing application in the nonlinear dynamics and static analysis, the potential of the ANCF method in the nonlinear postbuckling and buckling analysis needs further exploration. Some pioneering efforts in the direction of ANCF-based buckling analysis include works by several groups, as discussed subsequently. Luo *et al.* proposed a new hyper-elastic ANCF shell element utilizing the Kirchoff–Love theory and used the arc-length method to trace the whole nonlinear equilibrium path in

*** Corresponding author: Peng Lan,** School of Mechanical and Electrical Engineering, Xi'an University of Architecture and Technology, Xi'an, Shanxi, 710055, China; State Key Laboratory of Green Building in Western China, Xian University of Architecture & Technology, Xi'an, Shanxi, 710055, China, e-mail: lan_p@sina.com
Abdur Rahman Shaukat: Department of Mechanical Engineering, University of Management and Technology, Sialkot Campus, Lahore, 51041, Pakistan
Jia Wang: School of Mechanical Engineering, Shenyang University of Technology, No. 111, Shenliao West Road, Shenyang, 110870, China
Tengfei Wang: State Key Laboratory for Strength and Vibration of Mechanical Structures, School of Aerospace Engineering, Xi'an Jiaotong University, West Xianning Road 28, Xi'an, 710049, China
Nianli Lu: School of Mechatronics Engineering, Harbin Institute of Technology, Harbin, China

the load–displacement space of the cylindrical shells [16]. Similarly, a new elastoplastic thin shell ANCF element based on the Kirchoff–Love theory and layered plastic model was introduced by Li *et al.* to predict the nonlinear response [17]. In these studies, the use of ANCF shell elements has been verified in the postbuckling analysis of the classical shell structure, but the ANCF beam element still needs to be assessed against the benchmark example for the postbuckling structural analysis. Nachbagauer *et al.* constructed a three-node beam element and traced the nonlinear equilibrium path of a right-angle frame under end force by utilizing the nonlinear static iteration method with a small perturbation load [18]. Nachbagauer and Gerstmayr used the enhanced continuum mechanics-based and structural mechanics-based formulation in the buckling analysis, while the standard continuum mechanics-based formulation was not assessed. Recently, Shaukat *et al.* tested three ANCF beam-based approaches in conjunction with the arc-length method on the in-plane nonlinear postbuckling of the circular arches [19]. In the meantime, Wang and Wang used the energy criterion-based dichotomy scheme to find the critical buckling load of the right angle frame [20]. The conceptual difference between the energy criterion-based dichotomy scheme and the other studies mentioned here is that the perfect geometric configuration is not destroyed while finding the critical buckling load. On the contrary, the arc-length method-based limit point postbuckling load solutions are bound to allow the large deformation for the algorithm to work. Hence, the perfect geometry is not preserved. In the current study, both methods of buckling load estimations are utilized to analyze the benchmark problem of the beam–column structure of Lee's frame.

A recent rise in interest in the nonlinear behavior of structures has led researchers to see the instability in a new light marking the shift from the "buckliphobia to buckliphilia" [21], some referring to it as "well-behaved nonlinear structure" [22], and others calling it "Happy Catastrophe" [23]. However, by using the mechanical instabilities of the new smart material design, new application areas can be explored in the direction of soft machines with sensing, actuating, and control capabilities [24]. Hence, it is imperative to keep exploring the use of advanced numerical techniques, especially of nonlinear beam models such as ANCF beam, which are more general than the Bernoulli–Euler and Timoshenko beam-based FEM models. For the time being, ANCF has been proven suitable to handle flexible beams, and it also provides straightforward integration between MBS and nonlinear FEM algorithms [25]. Although it completely supports the use of GCM-based nonlinear material laws [26–28]. Due to the above-mentioned favorable characteristics of ANCF, its use in the design of new smart material-based structures needs to be further explored. Comparatively, ANCF-based elastoplastic analysis can be useful for snap-based designing, shape morphing, and multi-stable mechanical components. In the future, ANCF can be a good numerical tool for snap-based designing. This study is a small step in this direction to show that ANCF can be successfully used to study the nonlinear buckling and postbuckling behavior of the framed structures. In addition, it can effectively trace the complex nonlinear equilibrium paths in the load–displacement space of Lee's frame.

The article aims to thoroughly assess the performance of the ANCF beam element on the nonlinear postbuckling and buckling analysis of the benchmark Lee's frame. To achieve this, the arc-length method and the energy criteria method are implemented. The standard continuum mechanics-based lower-order beam element/higher-order beam element (HOBE) and the modified one using two locking alleviation methods are tested and compared. The study proves ANCF as a new tool that can be effectively used in the future to explore the nonlinear space for the snap-based design of flexible, soft smart structures, sensors, actuators, or energy-harvesting mechanisms.

The article is organized as follows: In Section 2, a brief literature review of frame analysis and the motivation to use the physics-based ANCF is described. In Section 3, the ANCF beam element and the modified one using the locking alleviation methods are introduced. Subsequently, the nonlinear postbuckling and buckling analysis methods employed are presented in Section 4. In Section 5, the numerical cases in order to verify the capability of the ANCF beam elements for the nonlinear postbuckling and buckling analysis of Lee's frame are presented. In Section 6, the conclusion is drawn based on the gathered insights.

2 Overview of postbuckling analysis of frames

The slender frames are used in mechanical, civil, and aerospace engineering design [29]. Early researchers such as Timoshenko and Gere systematically studied the buckling of the right-angle frame using the analytical method [30]. Then, Koiter showed the imperfection sensitivity of the load-carrying simple frames by applying the perturbation technique [31]. Later, Roorda and Chilver utilized first- and second-order perturbation to estimate the bifurcation loads for the two-bar problem [32]. Lee *et al.* were the first to obtain the nonlinear path for the frame deflection by using the numerical technique of the modified Newton–Raphson

method. The numerical example studied by Lee *et al.* became the benchmark now commonly referred to as "Lee's frame" [33]. Akoush *et al.* obtained the critical buckling loads and the nonlinear equilibrium path for the framed structures utilizing incremental nonlinear analysis. The nonlinear strain–displacement relationships were used with the continuous updating of the stiffness matrix to incorporate the nonlinear geometric effects [34]. Parametric nonlinear analysis was done on rotationally constrained rigid jointed frames, which are loaded symmetrically and asymmetrically, to study the effects of load eccentricity and slenderness ratio by Simitses *et al.* [35–37]. Pignataro and Rizzi investigated the local and global buckling modes exhibiting unstable postbuckling behavior by conducting the imperfection sensitivity of the asymmetric portal frame. It was found that the presence of multiple buckling modes enhances the imperfection sensitivity of the portal frame [38–40]. Pacsote and Eriksson compared the total Lagrangian-based element against the co-rotational based beam element approaches in their study of the nonlinear postbuckling analysis of the framed structures. It was found that there is no considerable difference in the results for the large deformation cases of moderate nature [41]. Waszczyszyn and Janus-Michalska used the exact finite elements (EFEs) by directly integrating the complete field equations obtained from formulating two-point boundary value problem. They found that the number of elements required in the in-plane nonlinear analysis of the slender frames using EFEs is less than using standard finite elements [42]. The effect of initial imperfections, geometric properties, and boundary conditions on the nonlinear postbuckling behavior of the frame structure was studied in detail by Galvão *et al.* to help improve the engineering design and analysis of elastic frames [43]. Basaglia *et al.* used generalized beam theory-based beam finite elements to study the local, distortional, and global postbuckling behavior of thin-walled steel frames [44]. Yeong-Bin and Shyh-Rong studied extensively the nonlinear behavior of the framed structures under compressive loads and different boundary conditions [45]. In their recent article, they summarized the different analytical techniques and numerical methods utilized to study the frames [46]. They also pointed out that if the physics-based finite element, along with the incremental-iterative arc-length method, is utilized to simulate the complex multi-loop nonlinear postbuckling behavior, the overall process can be made simpler and more effective. As the physics-based finite element completely respects the rigid body displacements at each step, making the overall efficiency much better. Hence, this study is conducted to evaluate the feasibility and effectiveness of ANCF in nonlinear frame analysis.

3 Theoretical background of ANCF

Absolute nodal coordinates and nodal slopes are used in the discretization scheme built in the framework of ANCF. Therefore, infinitesimal and finite rotation assumptions which are used in the infinitesimal rotation elements, large rotation vector elements, and incremental-rotation corotational formulations are relaxed. Consequently, the mass matrix remains constant in the equation of motion. Additionally, the Coriolis and centrifugal forces become zero in the equation of motion [2]. The large displacement, large rotation, and large deformation analysis by means of ANCF require straightforward implementation [14]. For the sake of convenience, the four ANCF-based approaches being utilized in this study are briefly outlined in the following sub-sections.

3.1 Omar-Shabana beam element (OmSh)

The standard two-dimensional shear deformable ANCF beam element in which elastic forces are derived using the GCM approach is abbreviated as "OmSh" in this study [47]. For this OmSh element, the assumed displacement field in the global coordinate system is defined as follows:

$$\mathbf{r} = \begin{bmatrix} a_0 + a_1x + a_2y + a_3xy + a_4x^2 + a_5x^3 \\ b_0 + b_1x + b_2y + b_3xy + b_4x^2 + b_5x^3 \end{bmatrix}. \tag{1}$$

Then, the position vector of an arbitrary point on the beam is obtained by $\mathbf{r} = \mathbf{S}(\mathbf{x})\mathbf{e}$, where $\mathbf{x}$ is the material coordinate vector in the straight configuration and $\mathbf{e}$ is the vector of nodal coordinates given by

$$\left.\begin{aligned} \mathbf{e} &= [\mathbf{e}^{1\mathrm{T}}\,\mathbf{e}^{2\mathrm{T}}]^{\mathrm{T}} \\ \mathbf{e}^i &= [\mathbf{r}^{i\mathrm{T}}\,\mathbf{r}_x^{i\mathrm{T}}\,\mathbf{r}_y^{i\mathrm{T}}]^{\mathrm{T}}\; i = 1, 2 \end{aligned}\right\}. \tag{2}$$

The element has two nodes, while the position vector $\mathbf{r}^i$ and the two gradient vectors $\mathbf{r}_x^i = \partial\mathbf{r}^i/\partial x$ and $\mathbf{r}_y^i = \partial\mathbf{r}^i/\partial y$, $i = 1, 2$ are used as DOFs, where x and y are the material coordinates in the straight configuration. The matrix of shape functions is given by

$$\mathbf{S} = [s_1\mathbf{I} \quad s_2\mathbf{I} \quad \ldots \quad s_6\mathbf{I}], \tag{3}$$

where $\mathbf{I}$ is the identity matrix and $s_i (i = 1, 2, \ldots, 6)$ are shape functions:

$$\left.\begin{aligned} s_1 = 1 - 3\xi^2 + 2\xi^3, \quad s_2 = l(\xi - 2\xi^2 + \xi^3), \quad s_3 = l(\eta - \xi\eta) \\ s_4 = 3\xi^2 - 2\xi^3, \quad s_5 = l(-\xi^2 + \xi^3), \quad s_6 = l\xi\eta \end{aligned}\right\}, \tag{4}$$

where ξ and η are the dimensionless bi-normalized element coordinates and l is the length of the beam element in the initial reference configuration. The bi-normalized coordinates are $\xi = x/l$ and $\eta = y/l$, where $0 \le x \le l$ and $-h/2 \le y \le h/2$, h is the height of the element. According to the GCM approach, the matrix of the position vector gradients (Jacobian matrix) or the deformation gradient is given by

$$\mathbf{J} = \mathbf{J}_e\mathbf{J}_0^{-1} = \frac{\partial \mathbf{r}}{\partial \mathbf{X}} = \frac{\partial \mathbf{r}}{\partial \mathbf{x}}\left(\frac{\partial \mathbf{X}}{\partial \mathbf{x}}\right)^{-1}, \tag{5}$$

where $\mathbf{X} = \mathbf{S}(\mathbf{x})\mathbf{e}_0$ represents the element parameters in the initial reference configuration, $\mathbf{J}_e = \partial \mathbf{r}/\partial \mathbf{x}$ and $\mathbf{J}_0 = \partial \mathbf{X}/\partial \mathbf{x}$. The Green–Lagrange strain matrix is obtained as follows:

$$\boldsymbol{\varepsilon}_m = \frac{1}{2}(\mathbf{J}^{\mathrm{T}}\mathbf{J} - \mathbf{I}), \tag{6}$$

where $\mathbf{I}$ is the identity matrix and the strain in Voigt is written as follows:

$$\varepsilon_v = [\varepsilon_{xx} \quad \varepsilon_{yy} \quad 2\varepsilon_{xy}]^{\mathrm{T}}, \tag{7}$$

where ε_{xx}, ε_{yy}, and ε_{xy} represent the axial, transverse, and shear strains, respectively. For the linearly elastic material, the strain energy is calculated using the following relation:

$$U = \frac{1}{2}\int_V \boldsymbol{\varepsilon}_v^{\mathrm{T}}\mathbf{E}_m\boldsymbol{\varepsilon}_v \det(\mathbf{J}_0)\mathrm{d}V, \tag{8}$$

where $\det(\mathbf{J}_0)$ indicates the determinant of $\mathbf{J}_0$, V indicates straight configuration volume, and $\mathbf{E}_m$ is the matrix of elastic coefficients. The plane stress assumption is adopted as follows:

$$\mathbf{E}_m = \frac{E}{1-\nu^2}\begin{bmatrix} 1 & \nu & 0 \\ \nu & 1 & 0 \\ 0 & 0 & (1-\nu)/2 \end{bmatrix}, \tag{9}$$

where E is Young's modulus and ν is Poisson's ratio. The stress vector from the mechanics definition is calculated as follows:

$$\boldsymbol{\sigma}_v = \mathbf{E}_m\boldsymbol{\varepsilon}_v. \tag{10}$$

The elastic force can be obtained by differentiating the elastic energy with respect to the nodal vector as follows:

$$\mathbf{Q}_s = \frac{\partial U}{\partial \mathbf{e}} = \int_V \left(\frac{\partial \varepsilon_v}{\partial \mathbf{e}}\right)^{\mathrm{T}} \boldsymbol{\sigma}_v |\mathbf{J}_0| \mathrm{d}V. \tag{11}$$

Then, the tangential stiffness matrix will be obtained by derivation of elastic force by the nodal coordinate vector as follows:

$$\begin{aligned}\mathbf{K} = \frac{\partial \mathbf{Q}_s}{\partial \mathbf{e}} = \int_V \Bigg[&\left(\frac{\partial^2 \boldsymbol{\varepsilon}_v(1)}{\partial \mathbf{e}^2}\right)\boldsymbol{\sigma}_v(1) + \left(\frac{\partial^2 \boldsymbol{\varepsilon}_v(2)}{\partial \mathbf{e}^2}\right)\boldsymbol{\sigma}_v(2) \\ &+ \left(\frac{\partial^2 \boldsymbol{\varepsilon}_v(3)}{\partial \mathbf{e}^2}\right)\boldsymbol{\sigma}_v(3) + \left(\frac{\partial \boldsymbol{\varepsilon}_v}{\partial \mathbf{e}}\right)^T \boldsymbol{\sigma}_v \left(\frac{\partial \boldsymbol{\varepsilon}_v}{\partial \mathbf{e}}\right)\Bigg] \mathrm{d}V,\end{aligned} \tag{12}$$

where the numbers represent the position of stress and strain component in the corresponding vectors.

3.2 Omar–Shabana beam element with Strain Split Method (OS-SSM)

SSM was originally proposed by Patel and Shabana in order to alleviate the locking problem present in the standard Omar–Shabana ANCF beam element [48]. For the SSM approach, the assumed displacement field equations remain as shown in Eq. (1). This approach is abbreviated as "OS-SSM" in this study. Locking alleviation was achieved by decoupling the higher-order strain terms found in the axial strain and the transverse strain. In this approach, the position field of the beam element is defined as follows:

$$\mathbf{r} = \mathbf{r}^c + y\mathbf{r}_y\,, \quad \mathbf{r}_x = \mathbf{r}_x^c + y\mathbf{r}_{yx}\,, \quad \mathbf{r}_y = \mathbf{r}_y, \tag{13}$$

where the superscript c represents the centerline of the beam and the matrix of the position vector gradients is defined as follows:

$$\begin{aligned}\mathbf{J} &= [\mathbf{r}_x \quad \mathbf{r}_y] = [\mathbf{r}_x^c + y\mathbf{r}_{yx} \quad \mathbf{r}_y] = [\mathbf{r}_x^c \quad \mathbf{r}_y] + [y\mathbf{r}_{yx} \quad \mathbf{r}_y] \\ &= \mathbf{J}^c + \mathbf{J}^k,\end{aligned} \tag{14}$$

where $\mathbf{J}^c$ represents terms belonging to the centerline of the beam and $\mathbf{J}^k$ represents terms belonging to higher-order terms associated with the shear deformation and curvature of the beam element. The Green–Lagrange strain tensor is defined as $\boldsymbol{\varepsilon} = \boldsymbol{\varepsilon}^c + \boldsymbol{\varepsilon}^k$, and the two strains are given as follows:

$$\left.\begin{aligned}\boldsymbol{\varepsilon}^c &= \frac{1}{2}(\mathbf{J}^{cT}\mathbf{J}^c - \mathbf{I}) \\ \boldsymbol{\varepsilon}^k &= \frac{1}{2}(\mathbf{J}^{cT}\mathbf{J}^k + \mathbf{J}^{kT}\mathbf{J}^c + \mathbf{J}^{kT}\mathbf{J}^k)\end{aligned}\right\}. \tag{15}$$

The second Piola–Kirchoff stress in the Voigt form is expressed as $\boldsymbol{\sigma}_v = \mathbf{E}^c\boldsymbol{\varepsilon}_v^c + \mathbf{E}^k\boldsymbol{\varepsilon}_v^k$, where strains are also written in Voigt form. In addition, $\mathbf{E}^k = \mathrm{diag}(E, E, \mu k_s)$ while utilizing the plane strain assumption $\mathbf{E}^c$ is defined as follows:

$$\mathbf{E}^c = \begin{bmatrix} \lambda + 2\mu & \lambda & 0 \\ \lambda & \lambda + 2\mu & 0 \\ 0 & 0 & \mu k_s \end{bmatrix}, \tag{16}$$

where λ and μ are Lamé parameters, E is Young's modulus, and ν is Poisson's ratio, whereas $k_s = 10(1+\nu)/(12+11\nu)$ is the shear correction coefficient. The strain energy is given by

$$U = \frac{1}{2}\int_V \boldsymbol{\varepsilon}_v^T(\mathbf{E}^c\boldsymbol{\varepsilon}_v^c + \mathbf{E}^k\boldsymbol{\varepsilon}_v^k)|\mathbf{J}_0|\mathrm{d}V = \frac{1}{2}\int_V \varepsilon_v^T\boldsymbol{\sigma}_v|\mathbf{J}_0|\mathrm{d}V. \tag{17}$$

The strain energy in the form of stress and strain vector is shown in the above equation. Then, the elastic force and tangential stiffness matrix are calculated using the formulation shown in Section 3.1. Complete derivation for SSM and further details about how to use it for curved geometries can be found in the study of Patel and Shabana [48].

3.3 Enhanced continuum mechanics formulation (OS-EnCM)

The standard Omar–Shabana (OmSh) beam element has been found to have Poisson locking because of the axial strain and transverse strain coupling in the energy formulation. To avoid this, Gerstmayr *et al.* [49] proposed the method known as enhanced continuum mechanics formulation in which the strain energy is calculated in two parts. In this way, the Poisson effect is excluded in the transverse direction, and the Poisson effect is included only in the beam centerline. This approach is utilized in the Omar–Shabana beam element framework, hence, abbreviated as "OS-EnCM." The assumed displacement field equation for this approach is shown in Eq. (1). The formulation for strain energy is as follows:

$$U = \frac{1}{2}b\int_{-h/2}^{h/2}\int_{0}^{l}\boldsymbol{\varepsilon}^{\mathrm{T}}\mathbf{D}^{0}\boldsymbol{\varepsilon}\mathrm{d}x\,\mathrm{d}y + \frac{1}{2}bh\int_{0}^{l}\boldsymbol{\varepsilon}^{\mathrm{T}}\mathbf{D}^{v}\boldsymbol{\varepsilon}\mathrm{d}x, \tag{18}$$

where b is the thickness of the element; the first part excludes the Poisson effect with the help of the modified matrix of elastic coefficients given as follows:

$$\mathbf{D}^{0} = \begin{bmatrix} E & 0 & 0 \\ 0 & E & 0 \\ 0 & 0 & Gk_s \end{bmatrix}, \tag{19}$$

where $G = E/2(1+\nu)$ is the shear modulus. And, the matrix of elastic coefficients for the second part is formulated as follows:

$$\mathbf{D}^{v} = \frac{E\nu}{1-\nu^2}\begin{bmatrix} \nu & 1 & 0 \\ 1 & \nu & 0 \\ 0 & 0 & 0 \end{bmatrix}, \tag{20}$$

which includes the Poisson effect in the transverse direction. Then, the elastic force vector is given as follows:

$$\mathbf{Q}_s = \frac{\partial U}{\partial \mathbf{e}} = b\int_{-h/2}^{h/2}\int_{0}^{l}\int_{0}^{l}\left(\frac{\partial \boldsymbol{\varepsilon}_v}{\partial \mathbf{e}}\right)^{T}\boldsymbol{\sigma}^{0}\mathrm{d}x\mathrm{d}y + bh\int_{0}^{l}\left(\frac{\partial \boldsymbol{\varepsilon}_v}{\partial \mathbf{e}}\right)^{T}\boldsymbol{\sigma}^{v}\mathrm{d}x, \tag{21}$$

where $\boldsymbol{\sigma}^{0} = \mathbf{D}^{0}\boldsymbol{\varepsilon}$ and $\boldsymbol{\sigma}^{v} = \mathbf{D}^{v}\boldsymbol{\varepsilon}$. The tangential stiffness matrix is given as follows:

$$\begin{aligned}\mathbf{K}_1 = b\int_{-h/2}^{h/2}\int_{0}^{l}\Bigg[&\left(\frac{\partial^2 \boldsymbol{\varepsilon}_v(1)}{\partial \mathbf{e}^2}\right)^{\mathrm{T}}\boldsymbol{\sigma}^{0}(1) + \left(\frac{\partial^2 \boldsymbol{\varepsilon}_v(2)}{\partial \mathbf{e}^2}\right)^{\mathrm{T}}\boldsymbol{\sigma}^{0}(2) \\ &+ \left(\frac{\partial^2 \boldsymbol{\varepsilon}_v(3)}{\partial \mathbf{e}^2}\right)^{\mathrm{T}}\boldsymbol{\sigma}^{0}(3) + \left(\frac{\partial \boldsymbol{\varepsilon}_v}{\partial \mathbf{e}}\right)^{\mathrm{T}}\boldsymbol{\sigma}^{0}\left(\frac{\partial \boldsymbol{\varepsilon}_v}{\partial \mathbf{e}}\right) \\ &+ \left(\frac{\partial \boldsymbol{\varepsilon}_v}{\partial \mathbf{e}}\right)^{\mathrm{T}}\boldsymbol{\sigma}^{0}\left(\frac{\partial \boldsymbol{\varepsilon}_v}{\partial \mathbf{e}}\right)\Bigg]\mathrm{d}x\mathrm{d}y,\end{aligned} \tag{22}$$

$$\begin{aligned}\mathbf{K}_2 = \int_{0}^{l}\Bigg[&\left(\frac{\partial^2 \boldsymbol{\varepsilon}_v(1)}{\partial \mathbf{e}^2}\right)^{\mathrm{T}}\boldsymbol{\sigma}^{v}(1) + \left(\frac{\partial^2 \boldsymbol{\varepsilon}_v(2)}{\partial \mathbf{e}^2}\right)^{\mathrm{T}}\boldsymbol{\sigma}^{v}(2) \\ &+ \left(\frac{\partial^2 \boldsymbol{\varepsilon}_v(3)}{\partial \mathbf{e}^2}\right)^{\mathrm{T}}\boldsymbol{\sigma}^{v}(3) + \left(\frac{\partial \boldsymbol{\varepsilon}_v}{\partial \mathbf{e}}\right)^{\mathrm{T}}\boldsymbol{\sigma}^{v}\left(\frac{\partial \boldsymbol{\varepsilon}_v}{\partial \mathbf{e}}\right)\Bigg]\mathrm{d}x,\end{aligned} \tag{23}$$

where the numbers show the components in the corresponding vectors. The total tangential stiffness matrix is the sum of the two as follows:

$$\mathbf{K} = \mathbf{K}_1 + \mathbf{K}_2. \tag{24}$$

3.4 Higher order beam element (HOBE)

In the locking alleviation article, Patel and Shabana also proposed a new two-dimensional HOBE with 16 DOFs [48]. The HOBE adopts cubic interpolation in the longitudinal direction and quadratic interpolation in the transverse direction. The higher order interpolation allows capturing the complex deformation modes and also allows curvature level continuity on the elemental nodes. The transverse strain does not remain constant, thus allowing the easing of the Poisson locking, especially in the large deformation analysis. This element can also be directly derived as a two-dimensional subset from the three-dimensional HOBE proposed by Shen *et al.* [50], which was later found to be useful in the study of lateral buckling by Orzechowski and Shabana [51]. For HOBEs, the assumed displacement field in the global coordinate system is defined as follows:

$$\mathbf{r} = \begin{bmatrix} a_0 + a_1x + a_2y + a_3\mathrm{xy} + a_4x^2 + a_5y^2 + a_6\mathrm{xy}^2 \\ \quad + a_7x^3 \\ b_0 + b_1x + b_2y + b_3\mathrm{xy} + b_4x^2 + b_5y^2 + b_6\mathrm{xy}^2 \\ \quad + b_7x^3 \end{bmatrix}. \tag{25}$$

The element nodal coordinate vector for the HOBE is defined as follows:

$$\left.\begin{aligned}\mathbf{e} &= [\mathbf{e}^{1\mathrm{T}}\,\mathbf{e}^{2\mathrm{T}}]^{\mathrm{T}} \\ \mathbf{e}^{\mathrm{i}} &= [\mathbf{r}^{\mathrm{i}\mathrm{T}}\,\mathbf{r}_x^{\mathrm{i}\mathrm{T}}\,\mathbf{r}_y^{i\mathrm{T}}\,\mathbf{r}_{yy}^{\mathrm{i}\mathrm{T}}]^{\mathrm{T}}\; i = 1, 2\end{aligned}\right\}. \tag{26}$$

Correspondingly, the element has the second-order gradient $\mathbf{r}^i_{yy} = \partial^2\mathbf{r}^i/\partial y^2$, $i = 1, 2$, as the nodal DOFs, besides $\mathbf{r}^i$, $\mathbf{r}^i_x$, $\mathbf{r}^i_y$ $i = 1, 2$ as in the standard element (OmSh). The matrix of shape functions is defined as follows:

$$\mathbf{S} = [s_1\mathbf{I} \quad s_2\mathbf{I} \quad \ldots \quad s_8\mathbf{I}], \tag{27}$$

where $\mathbf{I}$ is the identity matrix and s^i, $i = 1, 2, \ldots, 8$, are shape functions given as follows:

$$\left.\begin{aligned} &s_1 = 1 - 3\xi^2 + 2\xi^3,\ s_2 = l(\xi - 2\xi^2 + \xi^3),\\ &s_3 = l(\eta - \xi\eta),\ s_4 = l^2(\eta^2 - \xi\eta^2)/2\\ &s_5 = 3\xi^2 - 2\xi^3,\ s_6 = l(-\xi^2 + \xi^3),\ s_7 = l\xi\eta,\\ &s_8 = l^2(\xi\eta^2)/2 \end{aligned}\right\}. \tag{28}$$

The strain energy, elastic force, and stiffness matrix derivation follow the GCM-based approach. The strain energy for HOBE is given by

$$U = \frac{1}{2}\int_V \boldsymbol{\varepsilon}_v^T\mathbf{E}_m\boldsymbol{\varepsilon}_v \det(\mathbf{J}_0)\mathrm{d}V = \frac{1}{2}\int_V \boldsymbol{\varepsilon}_v^T\boldsymbol{\sigma}_v \det(\mathbf{J}_0)\mathrm{d}V. \tag{29}$$

Furthermore, elastic force and tangential stiffness matrix are calculated, as shown in Section 3.1.

3.5 Slope discontinuity modeling using ANCF

As the gradient is not continuous at the rigid joint of Lee's frame, it requires special attention. Therefore, the technique to model the slope discontinuity using ANCF finite element is briefly described here. The utilization of a constant coordinate transformation matrix to deal with the slope discontinuity in the ANCF modeling was demonstrated by Shabana and Mikkola [52]. Specifically, an additional global parameterization is introduced to unify the gradients on the intersection node k, where the gradients $\mathbf{e}^{ik}$ and $\mathbf{e}^{jk}$ in the associated elements i and j are transformed to the unified structural gradient $\mathbf{p}^k$ *via* the transformation matrix $\mathbf{T}^{ik}$ and $\mathbf{T}^{jk}$ as follows:

$$\mathbf{e}^{mk} = \mathbf{T}^{mk}\mathbf{p}^k, \tag{30}$$

where the transformation matrix $\mathbf{T}^{mk}$ at node k in the element m is obtained as follows:

$$\mathbf{T}^{mk} = \begin{bmatrix} \mathbf{I} & \mathbf{O} & \mathbf{O} \\ \mathbf{O} & c^{mk}_{1,1}\mathbf{I} & c^{mk}_{2,1}\mathbf{I} \\ \mathbf{O} & c^{mk}_{1,2}\mathbf{I} & c^{mk}_{2,2}\mathbf{I} \end{bmatrix}, \tag{31}$$

where the transformation coefficients $c^{\mathrm{mk}}_{l,n}$ $l, n = 1, 2$, are

$$c^{\mathrm{mk}}_{l,n} = \frac{\partial X^{\mathrm{mk}}_l}{\partial x_n} = \frac{\partial[\mathbf{S}_l(\xi^{\mathrm{mk}}, \eta^{\mathrm{mk}})\mathbf{e}^m_0]}{\partial x_n}, \tag{32}$$

where x_n, $n = 1, 2$, represent the first and second element coordinates, $\mathbf{S}_l$ is the lth row of the shape function matrix, ξ^{mk} and η^{mk} are the bi-normalized coordinates of node k in element m, and $\mathbf{e}^m_0$ is the coordinate of element m in the initial configuration. It should be noted that the transformation matrix is obtained in the initial reference configuration. As a result, $\mathbf{T}^{mk}$ is a constant matrix which is the valuable property provided by the ANCF. Complete details can be found in the original article referenced here [52].

3.6 Boundary conditions

For the boundary conditions used throughout this study, the following expressions are used. For the pinned boundary condition, the x and y components of the absolute nodal coordinate positions are constraints, so that it is pinned but can rotate:

$$\mathbf{B} = \begin{bmatrix} [\mathbf{0}]_{2\times2} & [\mathbf{0}]_{2\times1} \\ [\mathbf{0}]_{1\times2} & [\mathbf{I}]_{(n-2)\times(n-2)} \end{bmatrix}, \tag{33}$$

where n is the number of components in the nodal coordinate vector; for OmSh, OS-SSM, and OS-EnCM, its value is 12, whereas for HOBE, it is 16. For the fixed boundary condition, all the components of the nodal coordinate vector at that node are constraints, so that neither it can move nor can rotate as shown below:

$$\mathbf{B} = \begin{bmatrix} [\mathbf{0}]_{m\times m} & [\mathbf{0}]_{m\times1} \\ [\mathbf{0}]_{1\times m} & [\mathbf{I}]_{m\times m} \end{bmatrix}, \tag{34}$$

where m is half the number of components in the nodal coordinate vector $m = n/2$.

3.7 ANCF finite-element formulation for the framed structure

The nodal coordinate vector obtained from the different elements, as presented in the previous section, should be transformed. First, to incorporate the boundary conditions and secondly, to include the slope discontinuity in the right angle frame as shown:

$$\bar{\mathbf{e}}^j = \mathbf{T}^j\mathbf{B}^j\mathbf{e}^j. \tag{35}$$

Similarly, for the elastic force calculation, the two effects are included as follows:

$$\bar{\mathbf{Q}}_{\mathbf{s}}^{\mathbf{j}} = \mathbf{B}^{\mathbf{j}}\mathbf{T}^{\mathbf{j}}\mathbf{Q}_{\mathbf{s}}^{\mathbf{j}}. \tag{36}$$

And, the tangential stiffness matrix is shown below:

$$\bar{\mathbf{K}}^{\mathbf{t}} = \mathbf{T}^{\mathbf{j}^T}\mathbf{B}^{\mathbf{j}^T}\mathbf{K}^{\mathbf{t},\mathbf{j}}\mathbf{B}^{\mathbf{j}}\mathbf{T}^{\mathbf{j}}. \tag{37}$$

The equation of the virtual work of stresses according to the GCM theory can be obtained by utilizing the Green–Lagrange strain and the second Piola–Kirchoff stress as shown below:

$$\delta W_s^j = -\int_{V^j} \boldsymbol{\sigma}_{P2}^j \delta\boldsymbol{\varepsilon}^j \mathrm{d}V^j. \tag{38}$$

The virtual strain can be expressed as the virtual changes in the position vector gradients as follows:

$$\delta\boldsymbol{\varepsilon}^j = \frac{1}{2}[(\delta\mathbf{J}^{j^T})\mathbf{J}^j + \mathbf{J}^{j^T}(\delta\mathbf{J}^j)]. \tag{39}$$

The second Piola–Kirchoff stresses are calculated from the Green–Lagrange strains as follows:

$$\boldsymbol{\sigma}_{P2}^j = \mathbf{E}_m\boldsymbol{\varepsilon}^j, \tag{40}$$

where E is the matrix of the elastic coefficient used to define the constitutive relationship. Hence, the virtual work in Eq. (38) can be written as follows:

$$\delta W_s^j = -\frac{1}{2}\int_{V^j}(\mathbf{E}_m\boldsymbol{\varepsilon})[(\delta\mathbf{J}^{j^T})\mathbf{J}^j + \mathbf{J}^{j^T}(\delta\mathbf{J}^j)]\mathrm{d}V^j = -\mathbf{Q}_s^{j^T}\delta\mathbf{e}^j, \tag{41}$$

where Q_s is the vector of the elastics forces. The virtual work of an external force F acting at a point on the nodal coordinate vector can be found as follows:

$$\delta W_e^j = \mathbf{F}^{j^T}\delta\mathbf{r}_P^j = \mathbf{F}^{j^T}\mathbf{S}^j\delta\mathbf{e}^j = \mathbf{Q}_e^{j^T}\delta\mathbf{e}^j. \tag{42}$$

Hence, utilizing the principle of virtual work for the static analysis, one can write

$$\sum_{j=1}^{n}(\mathbf{Q}_s^j - \mathbf{Q}_e^j)^T\delta\mathbf{e}^j = 0. \tag{43}$$

After incorporating the boundary conditions and slope discontinuity, it can be expressed as follows:

$$\sum_{j=1}^{n}(\mathbf{T}^j\mathbf{B}^j\mathbf{Q}_s^j - \mathbf{T}^j\mathbf{B}^j\mathbf{Q}_e^j)^T\delta\mathbf{e}^j = 0. \tag{44}$$

Which for the equation of the static equilibrium can be written as follows:

$$\bar{\mathbf{Q}}_s - \bar{\mathbf{Q}}_e = 0. \tag{45}$$

The above equation describes the static equilibrium, which can be solved using the nonlinear solver such as the Newton–Raphson method or arc-length method. In this study for the nonlinear postbuckling analysis, it is solved using Crisfield's arc-length method.

4 Computational strategies

In this section, the computational strategies to utilize the ANCF approach for the nonlinear postbuckling analysis and buckling analysis of framed structures are presented. For the inplane nonlinear postbuckling analysis, the arc-length method is adopted. For the buckling analysis, a dichotomy scheme is utilized.

4.1 Nonlinear postbuckling analysis with arc-length method

In nonlinear FEM, the load–deflection response of arches is studied by using the nonlinear static solvers such as the Newton–Raphson method. In the 1970s, the arc-length method was proposed by Wempner in which the generalized arc-length constraint in the load–deflection space is used to solve the algebraic equations of the discrete system. These equations are derived from the differential equations of the nonlinear continuous system to overcome the limit points in incremental computations [53]. In the 1980s, Riks proposed a numerical method similar to Wempner's method; however, the nonlinear equilibrium path is obtained using the incremental procedure, which uses the length of the equilibrium path as a control parameter [54]. Crisfield proposed the modified form of Rik's method, sometimes known as Crisfield's arc-length method. In this method, the tangential stiffness matrix required to solve the nonlinear algebraic equations of the discretized form of system equations is identical to the one utilized in the full Newton–Raphson iteration method. The equation for the nonlinear static equilibrium is written in the following in the continuation method, usually called as the arc-length method [55]:

$$\bar{\mathbf{Q}}_s - \bar{\mathbf{Q}}_e = \mathbf{Q}_{\mathrm{in}}(e) - \lambda_{\mathrm{ext}}\mathbf{q}_{\mathrm{ext}} = 0, \tag{46}$$

where λ_{ext} is the variable scalar loading parameter for the external force, $\mathbf{q}_{\mathrm{ext}}$ is the constant directional vector for the external force $\mathbf{F}_{\mathrm{ext}} = \lambda_{\mathrm{ext}}\mathbf{q}_{\mathrm{ext}}$, and $\mathbf{Q}_{\mathrm{in}}(\mathbf{e})$ is the vector for the internal elastic force, which is the nonlinear function of the nodal coordinate vector. The above equation is different from the equation used in the full Newton–Raphson iteration method in the way that an additional scalar loading parameter λ_{ext} is introduced [56]. Therefore, the dimension of the variable displacement space N, now, turns into $N + 1$ variable load–displacement space. Using the benefit of the additional field available, the following equation of constraint was introduced by Crisfield:

$$\Delta \mathbf{u}^{\mathrm{T}} \Delta \mathbf{u} = \Delta l^2. \tag{47}$$

In the arc-length method implemented in this article, the incremental arc-length parameter Δl is kept constant throughout the computation of the whole equilibrium path, whereas $\Delta \mathbf{u}$ is the incremental displacement vector. The solution in the iteration step is found by following the arc defined by the arc-length parameter Δl in the variable load–displacement space. But, the constraint in the displacement space does not allow the solution to deviate from the overall cylindrical curve being followed. Hence, this method is sometimes called as "cylindrical arc-length method." The algorithm utilized in this article is presented in detail in the study of Shaukat *et al.* [19].

The value of arc-length parameter $\Delta l = 0.2$ was used as a constant in the algorithm for each case being studied. If the algorithm fails to follow the whole equilibrium path, the constant value was reduced by half, and the nonlinear postbuckling analysis was simulated again.

4.2 Buckling analysis using energy criterion

Wang and Wang applied the energy criterion to find the relative minimum of the total potential energy of the system in order to find the critical buckling load. They effectively used the nonlinear iterative algorithm based on the dichotomy scheme to find the critical buckling load of the structure using ANCF beam elements.

The energy criteria can be utilized to find the critical buckling load, as we can seek to find the condition where the static equilibrium does not exist by continuously updating the applied load. Hence, all the loading conditions where the change in the total potential energy is positive definite corresponds to the equilibrium position [57]. The total potential energy expressed in the form of Taylor's series is

$$U(e) = U(e_0) + \left| \sum_{i=1}^{n} \frac{\partial U}{\partial e} \right|_0 e_i + \frac{1}{2} \left| \sum_{i=1}^{n} \sum_{j=1}^{n} \frac{\partial U}{\partial e_i \partial e_j} \right|_0 e_i e_j + \ldots \tag{48}$$

Since, at the static equilibrium position, the first derivative remains zero. There will be no change in the initial configuration with respect to the applied load:

$$\left. \frac{\partial U}{\partial e} \right|_0 = 0. \tag{49}$$

Rearranging Eq. (48), putting the value of the first derivative, and ignoring all the higher-order terms in the Taylor series, we can arrive at the following expression:

$$U(e) - U(e_0) = 0 + \frac{1}{2} \left| \sum_{i=1}^{n} \sum_{j=1}^{n} \frac{\partial^2 U}{\partial e_i \partial e_j} \right|_0 e_i e_j + 0, \tag{50}$$

$$\Delta U = \frac{1}{2} \left| \sum_{i=1}^{n} \sum_{j=1}^{n} \frac{\partial^2 U}{\partial e_i \partial e_j} \right|_0 e_i e_j, \tag{51}$$

where the tangential stiffness matrix corresponds to the term in the above expression as follows:

$$\mathbf{K}_{ij} = \sum_{i=1}^{n} \sum_{j=1}^{n} \frac{\partial^2 U}{\partial e_i \partial e_j}. \tag{52}$$

The energy criterion states that the homogenous quadratic form of Eq. (50) remains positive definite for the stable equilibrium to exist. It can occur if and only if the determinant of the tangential stiffness matrix is all positive, which can be expressed as follows:

$$\det(\mathbf{K}_t) > 0. \tag{53}$$

From the above discussion, it occurs that as the system moves toward instability, the value of the determinant tends to seek zero value. As soon as it becomes zero, the system is no more stable. Hence, the instability condition becomes

$$\det(\mathbf{K}_t) = 0. \tag{54}$$

While the determinant of the tangential stiffness matrix can be calculated utilizing eigenvalues as follows:

$$\det(\mathbf{K}_t) = \prod_{n=1}^{m} \Lambda^m, \tag{55}$$

where the determinant is the product of all the eigenvalues of the matrix. Hence, the critical point can be found by carefully monitoring the sign of the eigenvalue of the tangent stiffness matrix by applying the delicate dichotomy scheme, which iterates the solution closer and closer to zero against the varying compressive load. In this way, the first, second, or third buckling loads, along with the buckling mode shapes, can be extracted. Further details and discussion can be found in the study of Wang and Wang [20].

5 Numerical examples

In this section, the nonlinear postbuckling and buckling analysis is conducted for Lee's frame with different boundary conditions. To find the relevant buckling load, for different boundary condition cases, both buckling estimation methods are employed. And, to check the validity of the ANCF-based approaches being employed, and to verify

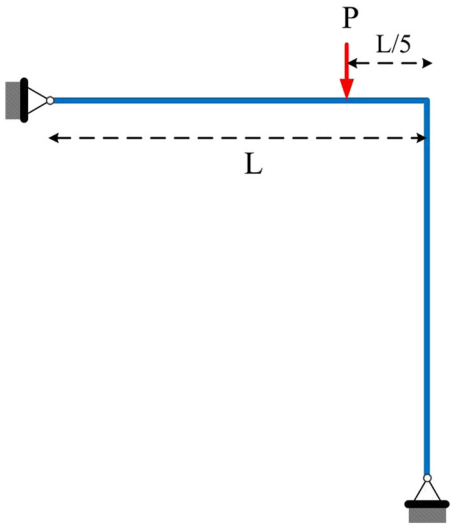

Figure 1: Lee's frame with pinned–pinned boundary conditions.

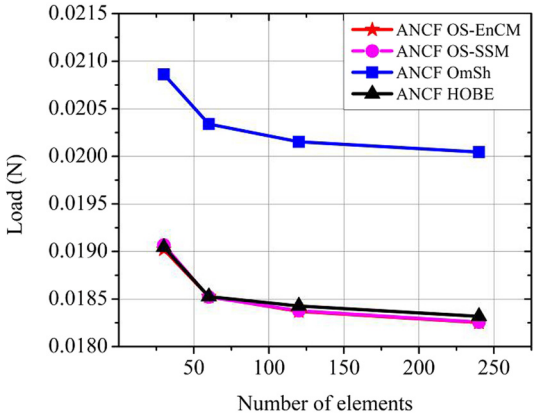

Figure 2: Convergence of ANCF elements.

the codes being used, the convergence for the nonlinear postbuckling limit load for Lee's frame (as shown in Figure 1) is studied, as shown in Figure 2. Throughout the study, the tolerance criterion and tolerance limit for the convergence to the equilibrium state are considered to be the Euclidean norm of the residual force as follows:

$$\|\mathbf{F}_{\text{ext}} - \mathbf{Q}_{\text{in}}\| \leq 1 \times 10^{-4}. \tag{56}$$

5.1 Case 1: Snap-back of Lee's frame

Lee's frame with the length of each arm $L = 0.120$ m, cross-sectional height $h = 0.002$ m, and cross-sectional width $b = 0.003$ m is considered. The material properties, *i.e.*, Young's modulus $E = 7.2 \times 10^6$ N/m^2 and Poisson's ratio $\nu = 0.3$, are used. In this case, pinned–pinned boundary conditions at the frame ends are assumed. The arc-length parameters used are $\Delta l = 0.2$ m with proscribed minimum and maximum load limits $-0.025 \leq P \leq 0.025$ N.

The total number of iterations and the number of load steps utilized to reach the maximum proscribed load when tracing the complete nonlinear equilibrium path for the OmSh, OS-SSM, OS-EnCM, and HOBE are shown in Table 1. The simulated deflection of Lee's frame can be seen in Figure 3, whereas *x*-deflection and *y*-deflection can be seen in Figures 4 and 5, respectively. The variation of strain energy according to the change in applied load is shown in Figure 6. The whole 3D equilibrium path using HOBE can be found in Figure 7. It can be observed that the OmSh slightly overpredicts the limit point postbuckling load as compared to the ANSYS BEAM188 reference solution. The results produced by the OS-SSM, OS-EnCM, and HOBE agree well with the reference solution. The complete snap-back nonlinear postbuckling response of Lee's frame with pinned–pinned boundary conditions is successfully predicted by ANCF-based approaches. However, it is found that the total number of iterations required to complete the path is minimum for the OmSh and then OS-EnCM. It is slightly higher for the OS-SSM and much higher for the HOBE. It should be further noted that the HOBE required only two iterations per incremental load step to reach the equilibrium state and does not present any convergence-related issues.

Table 1: Limit point postbuckling load for Lee's frame with pinned–pinned BCs (Case 1)

	OmSh	OS-SSM	HOBE	OS-EnCM	BEAM188
Limit point	0.020339	0.0185216	0.0185252	0.0185244	0.0185537
No. of elements	60	60	60	60	200
No. of steps	153	153	933	153	—
No. of iterations	438	738	1,866	448	—
Complete path	Yes	Yes	Yes	Yes	Yes

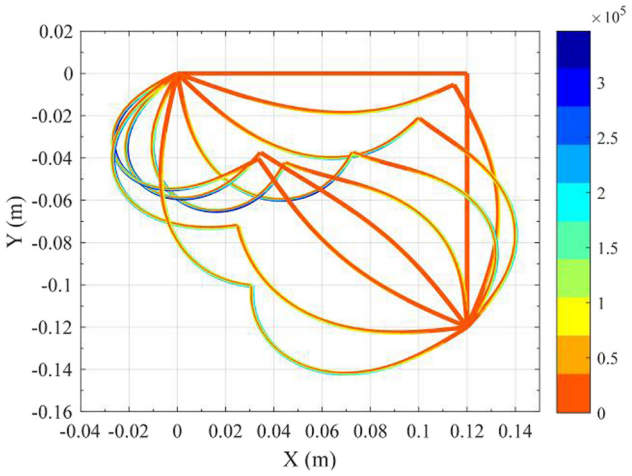

Figure 3: Lee's frame with pinned–pinned boundary conditions and contour represents von Mises stress (Case 1).

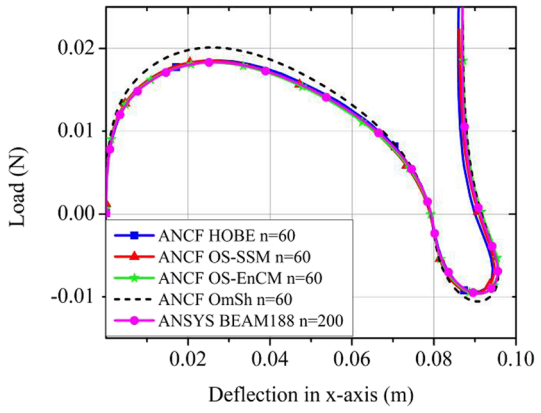

Figure 4: Snap-back of Lee's frame showing *x*-deflection (Case 1).

The buckling analysis based on the energy criterion utilizing the HOBE, OS-EnCM, and OmSh approaches is successfully conducted for Lee's frame with pinned–pinned boundary conditions. It is found that the OS-SSM failed to converge to the solution. Therefore, it is not included in Table 2. For comparison with the reference solution, 200 ANSYS BEAM188 elements are used to calculate the critical buckling load, and the obtained results are presented in Table 2. It can be seen that the ANCF-based HOBE and OS-EnCM results for the first, second, and third buckling loads are in good agreement with the reference, whereas the OmSh overpredicts the three buckling loads. The three buckling mode shapes simulated using the HOBE are shown in Figure 8.

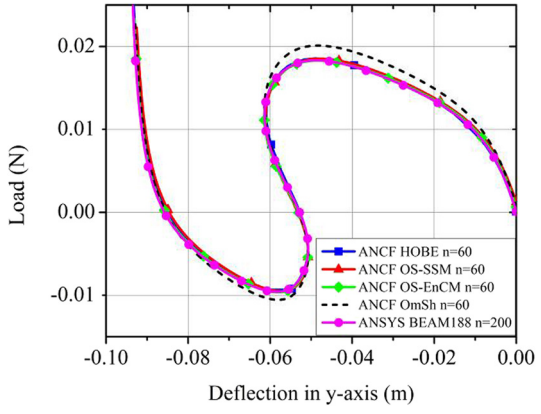

Figure 5: Snap-back of Lee's frame showing *y*-deflection (Case 1).

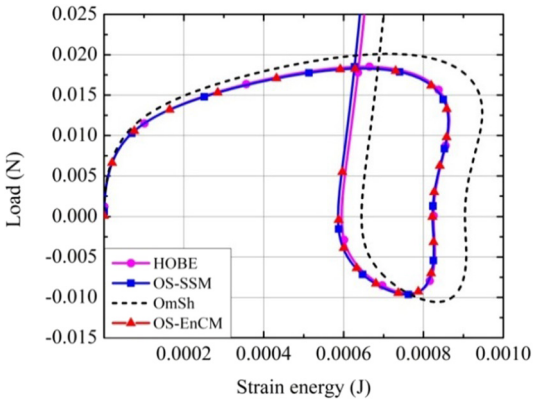

Figure 6: Strain energy of snap-back of Lee's frame (Case 1).

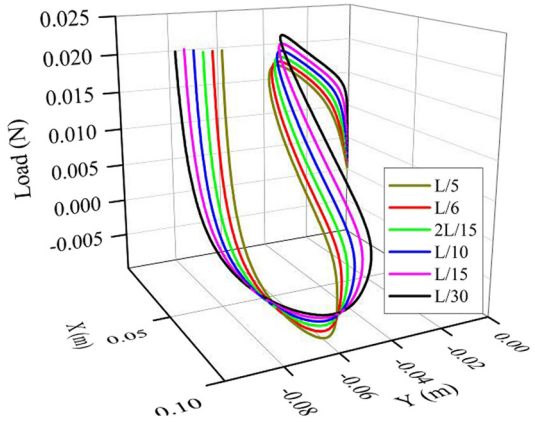

Figure 7: Complete 3D equilibrium path of snap-back of Lee's frame (Case 1) with varying offset load points.

Table 2: Critical buckling load for Lee's frame with pinned–pinned BCs (Case 1)

	First mode	Second mode	Third mode
ANCF HOBE	0.01384	0.04440	0.09504
ANCF OmSh	0.01538	0.04932	0.10450
ANCF OS-EnCM	0.01391	0.04434	0.09492
ANSYS BEAM188	0.01399	0.04487	0.09456

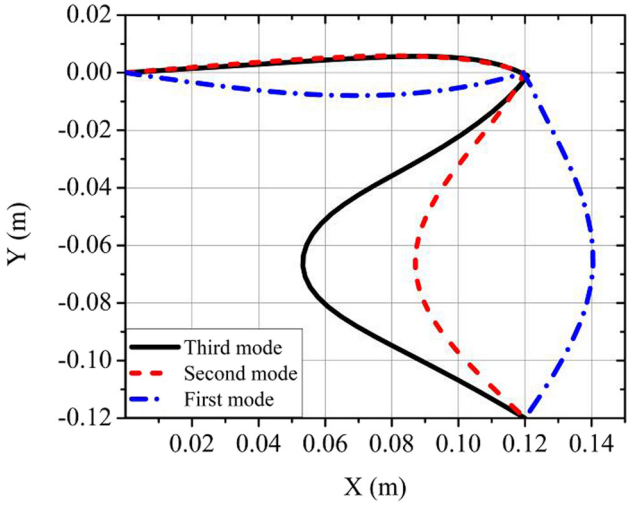

Figure 8: Buckling mode shapes for Lee's frame with pinned–pinned BCs (Case 1).

It should be noted that the energy criterion-based buckling analysis is done when the load is applied in the vertically downward direction at the rigid joint of Lee's frame, not offsetting by L/5, as in the nonlinear postbuckling analysis. Because the concept for using the buckling analysis is to model the perfect initial geometry with loading conditions of the structure without any imperfection, *i.e.*, without any introduction of small perturbation load or eccentric displacement in the form of a small offset. On the contrary, for the nonlinear postbuckling analysis, the nonlinear large deformation analysis is done by allowing the imperfection so that the whole nonlinear equilibrium path can be traced and the limit point postbuckling loads can be found. In further investigation, the HOBE approach is utilized while the offset point of the load is varied to find the lowest limit load, but L/5 is found to give the lowest value. Hence, we can see that the 0.0138 N critical buckling load is less than the 0.018 N limit point postbuckling load given by the L/5 offset. Therefore, the critical buckling load obtained by the energy criterion-based buckling analysis should be used as the maximum allowed load.

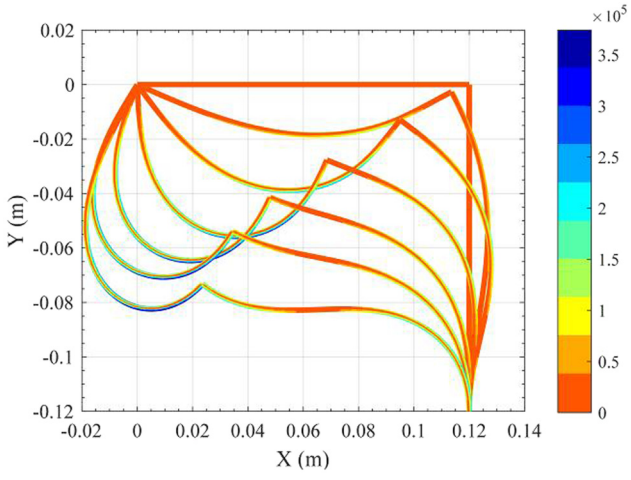

Figure 9: Lee's frame with pinned-fixed boundary conditions where contour represents von Mises stress (Case 2).

5.2 Case 2: Snap-through of Lee's frame

The whole nonlinear equilibrium path in the form of the snap-through response for Lee's frame with pinned-fixed boundary conditions is traced. The deflected frame after equal intervals can be seen in Figure 9, while the deflection in the *x*- and *y*-axis against load can be observed in Figures 10 and 11, respectively. The variation of strain energy according to the change in applied load is shown in Figure 12. The complete 3D equilibrium path using HOBE can be seen in

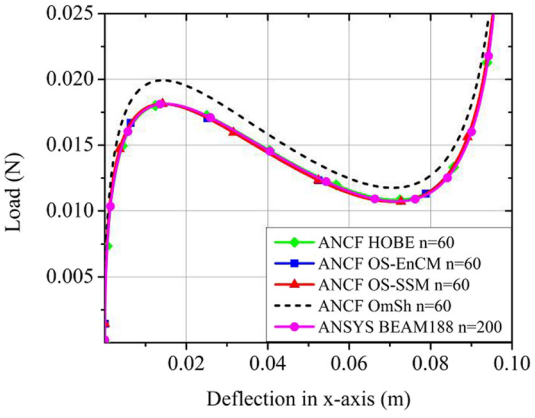

Figure 10: Snap-through of Lee's frame showing *x*-deflection (Case 2).

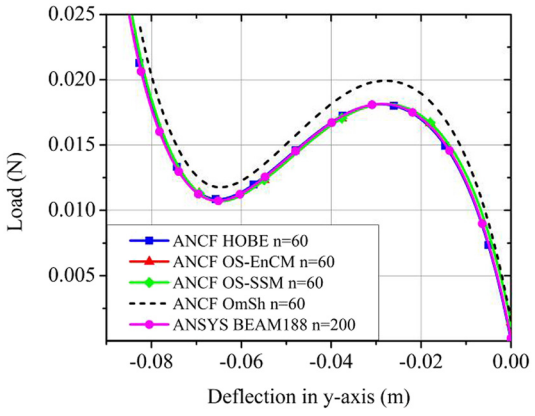

Figure 11: Snap-through of Lee's frame showing *y*-deflection (Case 2).

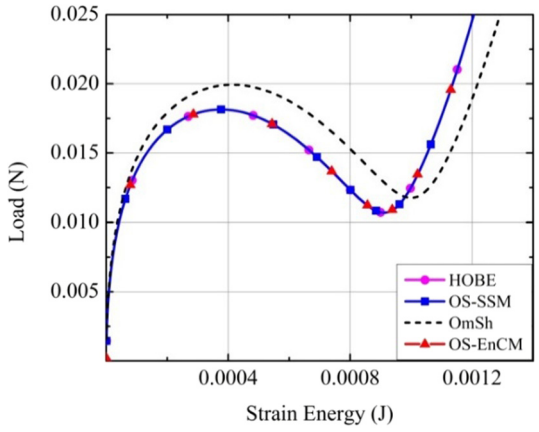

Figure 12: Strain energy graph of snap-through of Lee's frame (hinged-fixed).

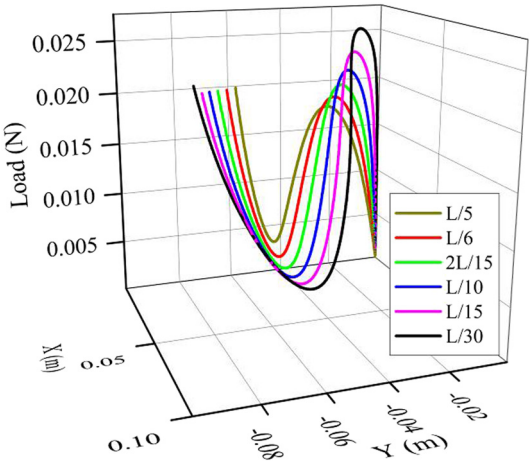

Figure 13: Complete 3D equilibrium path of snap-through of Lee's frame (Case 2) with varying offset load points.

Figure 13. The numerical results are presented in Table 3. It is observed from the data that the OmSh predicts a slightly higher limit load than the reference ANSYS BEAM188 solution due to the presence of the locking. Whereas the other ANCF-based approaches, *i.e.*, OS-SSM, OS-EnCM, and HOBE, have no considerable difference. The number of load steps and the total number of iterations required to complete the path are highest for the HOBE, high for the OS-SSM, while it is least for the OmSh and OS-EnCM. Additionally, it is important to notice that the OmSh, OS-EnCM, and HOBE only require two iterations per incremental load step to converge to the equilibrium state. The OS-SSM, in this case of snap-through buckling of Lee's frame, sometimes requires a higher number of iterations than two per incremental load step.

Similarly, as in the previous case, for the energy criterion-based buckling analysis OS-SSM failed to converge. But, the ANCF-based HOBE, OS-EnCm, and OmSh approaches converged, and the obtained solutions are shown in Table 4. The mode shapes obtained utilizing the HOBE approach are shown in Figure 14. The HOBE and OS-EnCM results for all three critical buckling loads match well with the ANSYS BEAM188 results, whereas, due to the locking phenomenon present in the OmSh element, the predicted critical load is higher.

Table 4: Critical buckling load for Lee's frame with pinned-fixed BCs (Case 2)

	First mode	Second mode	Third mode
ANCF HOBE	0.02709	0.06375	0.12581
ANCF OmSh	0.02979	0.07056	0.14070
ANCF OS-EnCM	0.02679	0.06351	0.12883
ANSYS BEAM188	0.02701	0.06397	0.12497

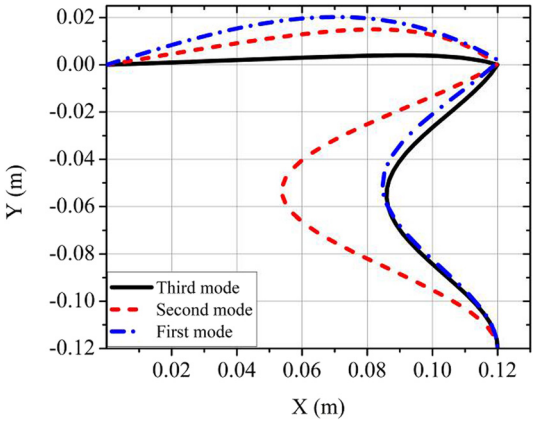

Figure 14: Buckling mode shapes for Lee's frame with pinned-fixed BCs (Case 2).

Table 3: Limit point postbuckling load for Lee's frame with pinned-fixed BCs (Case 2)

	OmSh	OS-SSM	HOBE	OS-EnCM	BEAM188
First limit point	0.019931	0.018145	0.018145	0.0181409	0.0181195
No. of elements	60	60	60	60	200
No. of steps	99	101	686	101	—
No. of iterations	198	466	1,372	202	—
Complete path	Yes	Yes	Yes	Yes	Yes

While using the HOBE approach, the offset point of the load is varied in the range of L/5 to L/30, but it was found that the L/5 offset gives the lowest value for the first limit load. After, the energy criterion-based buckling analysis and nonlinear postbuckling analysis results are compared. It is found that the first critical buckling load 0.027 N is higher than the postbuckling limit load 0.018 N, which means that the chance of limit point buckling occurring is higher. Therefore, the limit point postbuckling load should be used as the maximum allowed load.

5.3 Case 3: Lee's frame with looping phenomenon (fixed–fixed)

The first limit points of the nonlinear equilibrium path of Lee's frame with fixed–fixed boundary conditions are presented in Table 5. From the comparison of the OmSh, OS-EnCM, OS-SSM, and HOBE results against the ANSYS BEAM188, it can be seen that the OS-SSM failed to complete the whole nonlinear equilibrium path. Lee's frame deflections are simulated in Figure 15, while the x-deflection and y-deflection can be observed in Figures 16 and 17, respectively. The variation of strain energy according to the change in applied load is shown in Figure 18. The whole nonlinear equilibrium path is shown in Figure 19. The whole nonlinear equilibrium path using HOBE is shown in Figure 16. The HOBE results are produced using the arc-length parameter Δl = 0.2, whereas OmSh and OS-EnCM Δl = 0.1 are used. For OS-SSM arc-length parameter is further lowered to Δl = 0.05 even then it did not produce the whole path. For the OS-SSM approach, the first limit point is successfully attained, but the postbuckling behavior present in the form of the looping phenomenon is not captured. As in the previous cases, it can be observed that the OmSh slightly overpredicts the limit point postbuckling load. And, the ANCF-based HOBE and OS-EnCM predicted loads are in good agreement with the reference. On the contrary, it should be noted that the HOBE requires only two iterations per incremental load step to converge to the equilibrium state and successfully completes the whole equilibrium path without having any convergence issues.

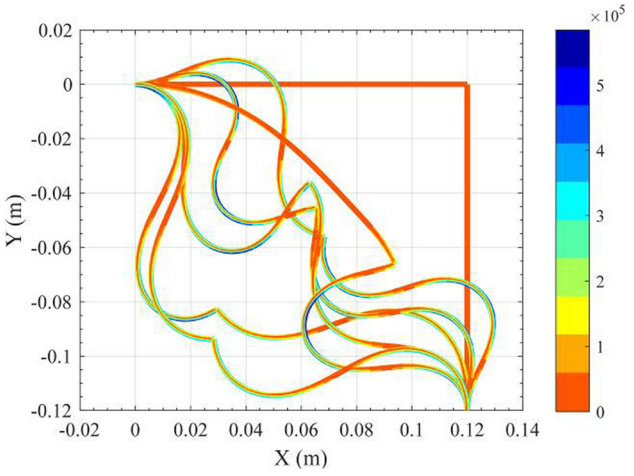

Figure 15: Lee's frame with fixed–fixed boundary conditions where contour represents von Mises stress (Case 3).

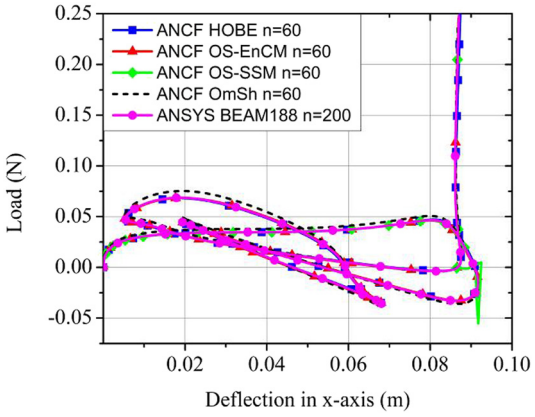

Figure 16: Lee's frame with looping phenomenon showing x-deflection (Case 3).

During the energy criterion-based buckling analysis, for Lee's frame with fixed–fixed boundary conditions, the ANCF-based OS-SSM element failed to converge. On the other hand, the ANCF-based OmSh, OS-EnCM, and

Table 5: Limit point postbuckling load for Lee's frame with fixed–fixed BCs (Case 3)

	OmSh	OS-SSM	HOBE	OS-EnCM	BEAM188
First limit point	0.050684	0.046235	0.046518	0.0461388	0.047132
No. of elements	60	60	60	60	200
No. of steps	982	515	6,242	983	—
No. of iterations	2,068	2,603	12,484	2,084	—
Complete path	Yes	No	Yes	Yes	Yes

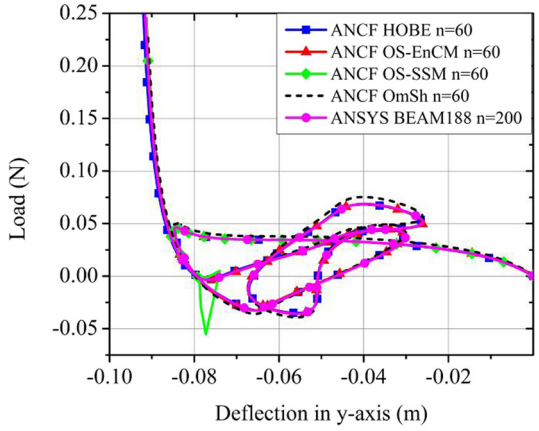

Figure 17: Lee's frame with looping phenomenon showing *y*-deflection (Case 3).

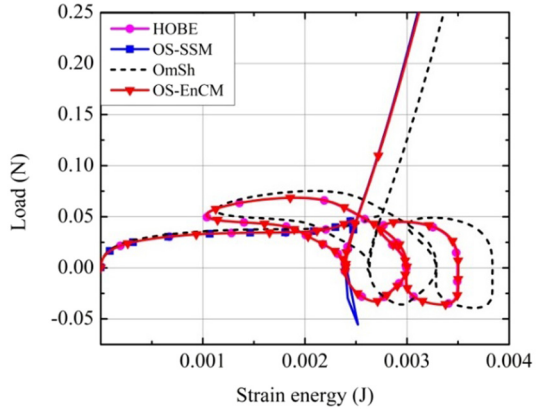

Figure 18: Strain energy graph of looping phenomenon of Lee's frame (Case 3).

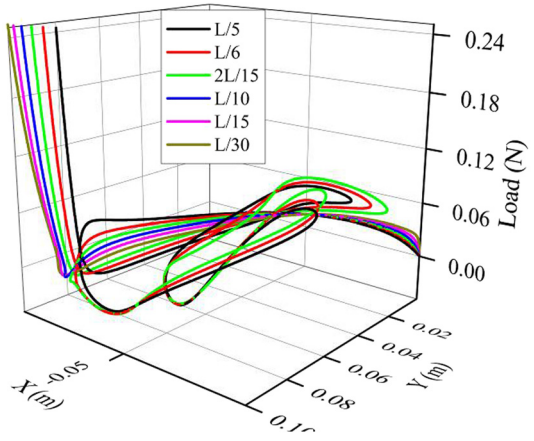

Figure 19: Complete 3D equilibrium path of looping phenomenon of Lee's frame (Case 3) with varying offset load points.

Table 6: Critical buckling load for Lee's frame with fixed–fixed BCs (Case 3)

	First mode	Second mode	Third mode
ANCF HOBE	0.02805	0.06575	0.12918
ANCF OmSh	0.03125	0.07206	0.14158
ANCF OS-EnCM	0.02820	0.06554	0.12867
ANSYS BEAM188	0.02873	0.06576	0.12827

HOBE give a result that agrees well with the ANSYS BEAM188-produced solution, as shown in Table 6. It can be seen that OmSh overpredicts the critical buckling loads. Hence, the three critical buckling loads and corresponding mode shapes are successfully extracted using HOBE. Three mode shapes obtained using the HOBE approach can be seen in Figure 20. While investigating the various offset load points, using the HOBE approach, it is found that the L/6 offset point gives the lowest first limit point load as 0.03395 N. As the lowest critical buckling load is 0.028 N which is less than the postbuckling limit load of the concern, the critical buckling load based on energy criterion should be used as the maximum allowed load.

5.4 Case 4: Lee's frame with looping phenomenon (fixed-pinned)

During the nonlinear postbuckling analysis, the looping behavior of Lee's frame with fixed-pinned boundary conditions is simulated, and numerical results are presented in Table 7. The deflected Lee's frame under loading is shown in Figure 21, whereas deflection graphs in the *x*- and *y*-axis can be observed in Figures 22 and 23,

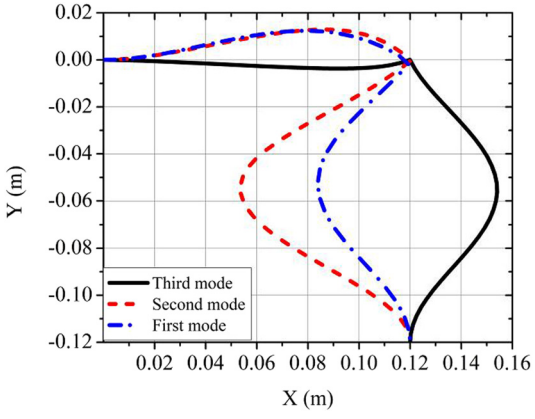

Figure 20: Buckling mode shapes for Lee's frame with fixed–fixed BCs (Case 3).

Table 7: Limit point postbuckling load for Lee's frame with fixed-pinned BCs (Case 4)

	OmSh	OS-SSM	HOBE	OS-EnCM	BEAM188
First limit point	0.071547	0.065528	0.065856	0.065265	0.065366
No. of elements	60	60	60	60	200
No. of steps	662	1,327	3,037	663	—
No. of iterations	1,324	3,766	6,074	1,326	—
Complete path	Yes	Yes	Yes	Yes	Yes

respectively. The variation of strain energy according to the change in applied load is shown in Figure 24. The complete 3D nonlinear equilibrium path obtained using HOBE is shown in Figure 25. The HOBE results are produced using the arc-length parameter as $\Delta l = 0.2$, whereas for OmSh and OS-EnCM $\Delta l = 0.1$ is used. For, the OS-SSM approach, arc-length parameter was further lowered to $\Delta l = 0.05$ in order to produce the whole path and it successfully traced the whole path. Nonetheless, the first limit points for the OmSh, OS-SSM, OS-EnCM, and HOBE are obtained and compared against the ANSYS BEAM188 reference solution. As, in the previous three cases, the OmSh approach slightly overpredicts the limit load due to the presence of locking. OS-SSM, OS-EnCM, and HOBE are found to be in good

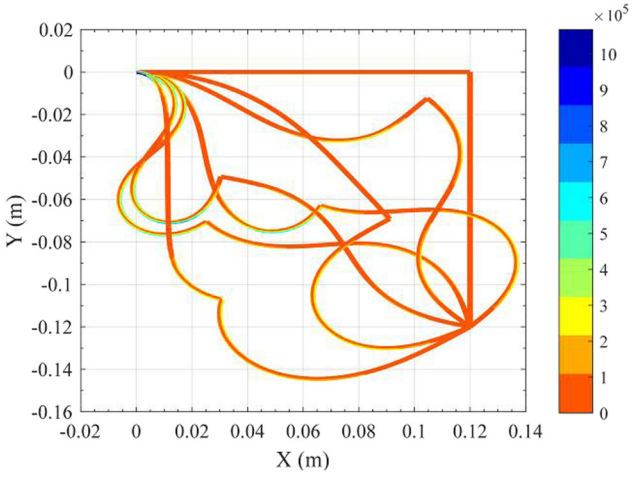

Figure 21: Lee's frame with fixed-pinned boundary conditions where contour represents von Mises stress (Case 4).

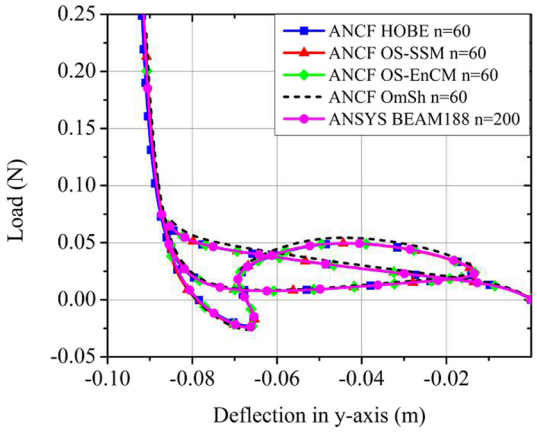

Figure 23: Lee's frame with looping phenomenon showing *y*-deflection (Case 4).

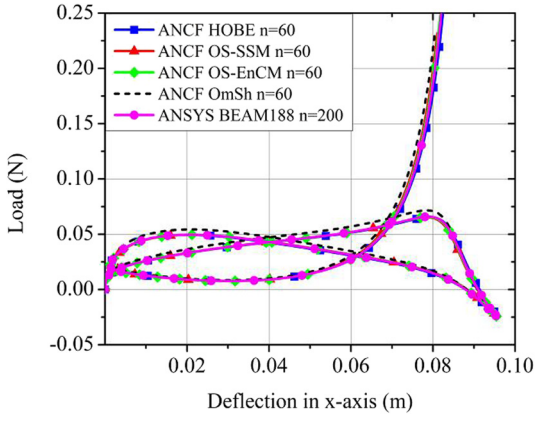

Figure 22: Lee's frame with looping phenomenon showing *x*-deflection (Case 4).

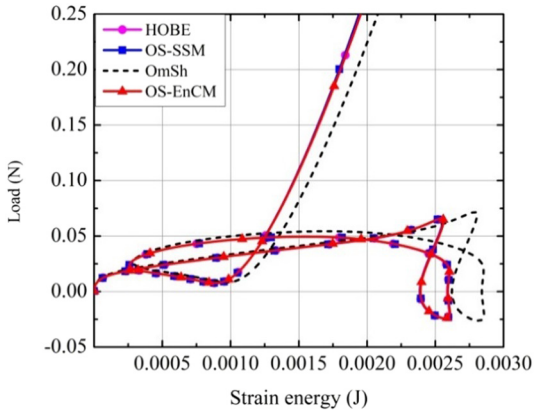

Figure 24: Strain energy graph of looping phenomenon of Lee's frame (Case 4).

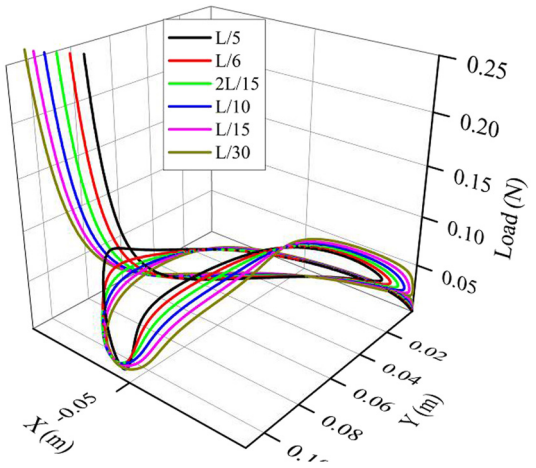

Figure 25: Complete 3D equilibrium path of looping phenomenon of Lee's frame (Case 4) with varying offset load points.

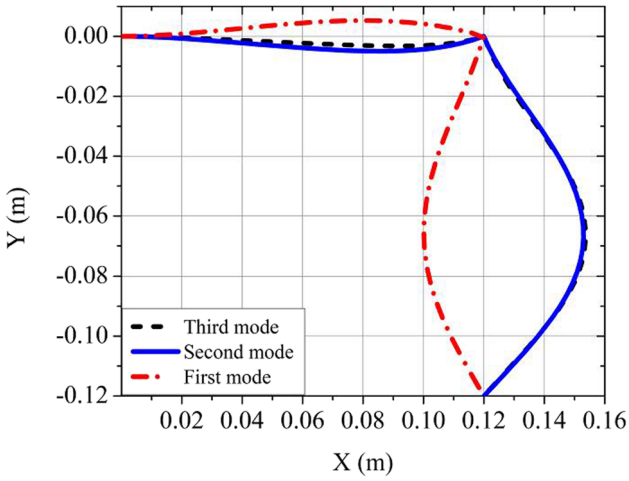

Figure 26: Buckling mode shapes for Lee's frame with fixed-pinned BCs (Case 4).

agreement with the reference ANSYS BEAM188 solution. On the contrary, it should be noted that the HOBE and OS-EnCM needed only two iterations per incremental load step while tracing the whole complex looping path and successfully completed it without presenting any convergence related issues.

In this case, the energy criterion-based buckling analysis for the OS-SSM element failed to converge. But, the ANCF-based HOBE, OS-EnCM, and OmSh approaches converged to the solution which is shown in Table 8. The result produced by the HOBE and OS-EnCM are found to be in good agreement with the ANSYS BEAM188 result for the three critical buckling loads. The three mode shapes using the HOBE approach are shown in Figure 26. Upon varying the offset load points and tracing the whole equilibrium path using the HOBE approach, it is found that the L/15 gives the lowest first limit load value as 0.04015 N. It is observed that the postbuckling limit load of concern is many times higher than the lowest critical buckling load of 0.014 N. Therefore, the maximum allowed load should not exceed the critical buckling load obtained by the energy criterion.

Table 8: Critical buckling load for Lee's frame with fixed-pinned BCs (Case 4)

	First mode	Second mode	Third mode
ANCF HOBE	0.01459	0.04626	0.09545
ANCF OmSh	0.01624	0.0509	0.1062
ANCF OS-EnCM	0.01460	0.04539	0.09664
ANSYS BEAM188	0.01490	0.04662	0.09705

5.5 Case 5: Roorda's frame

As it can be seen from the previous numerical problems, the ANCF-based HOBE approach is the best approach among the studied ANCF approaches for the nonlinear frame analysis. For further verification and validation, comparison with the experimental result is a must. Hence, the L-frame from Roorda's experiment is studied here.

Koiter, in his landmark thesis, applied the perturbation-based numerical technique to estimate the buckling load of the L-frame, which is given by the formula $P/P_{cr} = 1 - 0.3805\theta$. And, the buckling load is given by $P_{cr} = 1.407\pi^2 EI/L^2$. Rizzi *et al.* used a more sophisticated analytical approach incorporating up to fourth-order terms; the solution produced by them is $P/P_{cr} = 1 - 0.3805\theta + 0.4638\theta^2$. Further, Galvão *et al.* utilized an efficient nonlinear finite element formulation for the analysis of planar elastic frames together with a nonlinear

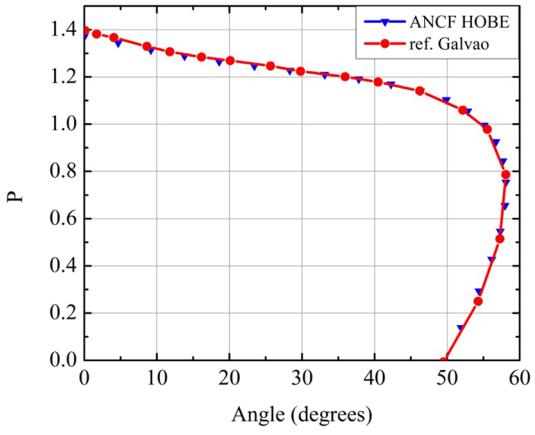

Figure 27: Postbuckling solution for the Roorda's frame.

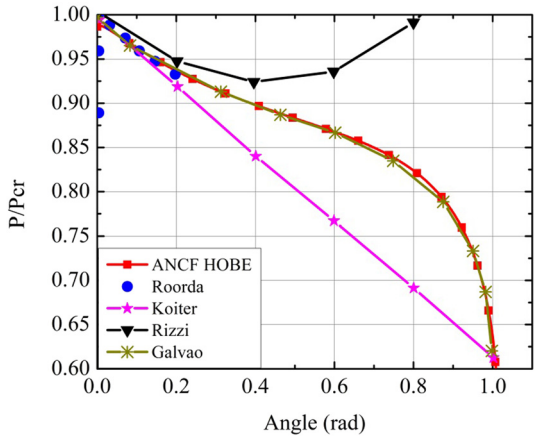

Figure 28: Comparison between ANCF based HOBE, Roorda's experiment, Koiter's perturbation technique, Rizzi's analytical solution and Galvão's nonlinear solution.

solution methodology. In Figures 27, amd 28 and data from Galvão's publication are used as a reference, which already contains Rizzi *et al.*, Koiter and Roorda results [43]. These reference results are then compared with 60 elements using the ANCF-based HOBE approach.

Rizzi *et al.* conducted a thorough parametric analysis of the two-bar frame problem by using the modified potential energy approach. This analysis was profound yet simple, allowing us to incorporate the fourth-order terms in the analytical solution. But, from Figures 27 and 28, when the analytical results of Rizzi, Roorda's experimental, and Koiter's perturbation approach are compared, it can be seen that Galvão's nonlinear solution and ANCF HOBE solution are much better.

6 Conclusion

This article verifies the capability of the ANCF beam element for the nonlinear postbuckling and buckling analysis of Lee's frame benchmark example. The GCM-based ANCF beam elements and the modified one using two locking alleviation methods are tested and compared. Four different boundary conditions, *i.e.*, pinned–pinned, fixed-pinned, pinned-fixed, and fixed–fixed, are studied. The nonlinear postbuckling behavior is traced in the form of snap-back, snap-through, and looping phenomenon while the corresponding limit point postbuckling loads are recorded. The energy criterion is applied by tracing the eigenvalues *via* the dichotomy scheme to find the critical buckling loads and extract the corresponding buckling mode shapes. All the obtained results are compared and discussed. The following conclusions can be reached:

1. The higher-order ANCF beam element based on the GCM approach (HOBE) is found to be accurate and stable among the approaches being investigated. It is also the consistent one, as it successfully converges to the solution without presenting any convergence-related issues for both types of buckling analysis. Additionally, for the nonlinear postbuckling analysis of the cases being investigated, HOBE needs only two iterations per incremental load step for convergence.
2. The standard ANCF beam element modified by the enhanced continuum mechanics method, *i.e.*, OS-EnCM, can predict the limit point postbuckling and critical buckling loads. But, during the two cases, the arc-length parameter needed to be adjusted and lowered to help the OS-EnCM approach to converge to the equilibrium path and trace the whole equilibrium path.
3. The standard ANCF beam element modified by the split strain method, *i.e.*, OS-SSM, during the nonlinear postbuckling analysis, can alleviate locking but is not able to trace the whole nonlinear equilibrium path for the fixed–fixed boundary condition case, which exhibits looping phenomenon. For the energy criterion-based buckling analysis of all Lee's frame cases being investigated, this approach does not converge to the solution.
4. The standard ANCF beam element based on the GCM approach, *i.e.*, OmSh, slightly overpredicts the limit load in the nonlinear postbuckling analysis due to the locking phenomenon but successfully traces the complete equilibrium path. For the energy criterion-based buckling analysis, this approach also slightly overpredicts the critical buckling load in all the boundary conditions being investigated.

Hence, it is concluded that the HOBE approach can be used for the general in-plane nonlinear postbuckling analysis and energy criterion-based buckling analysis of the frame structures with different boundary conditions. Whereas the OS-EnCM approach may reduce locking but should need attention while performing analysis. On the contrary, the OS-SSM approach may present some convergence-related issues, and the OmSh approach may slightly overpredict the buckling loads. Hence, the latter three approaches should be used with care.

Nomenclature

$\mathbf{e}$	vector of element nodal coordinates
$\mathbf{e}_0$	nodal vector in the reference configuration
x	longitudinal coordinate defined in the local coordinate system

y	transverse coordinate defined in the local coordinate system
l	length of the element
ξ	dimensionless longitudinal coordinate
η	dimensionless transverse coordinate
$\mathbf{r}$	global position vector of an arbitrary point between the nodes i and j
$\mathbf{r}^c$	absolute position vector of the centerline of the element
$\mathbf{r}_a$	slope of the absolute position vector defined as $\partial\mathbf{r}/\partial\alpha$ where $\alpha = x, y, yx$ or yy
s_i	shape function in the shape function matrix
$\mathbf{S}$	shape function matrix
$\mathbf{E}_m$	matrix of elastic coefficient
$\mathbf{E}^c$	matrix of material constants belongs to centerline terms
$\mathbf{E}^k$	matrix of material constants belongs to higher-order terms
$\mathbf{I}$	identity matrix of order two
$\mathbf{J}_0$	Jacobian matrix corresponding to a curved configuration
$\mathbf{J}_e$	Jacobian matrix corresponding to a deformed configuration
$\mathbf{J}$	Jacobian matrix of deformed configuration with respect to the curved configuration $\mathbf{J} = \mathbf{J}_e\mathbf{J}_0^{-1}$
$\mathbf{J}^c$	Jacobian matrix related to the centerline of the beam
$\mathbf{J}^k$	Jacobian matrix related to higher-order terms
$\boldsymbol{\varepsilon}_v$	Voigt strain
ε_{xx}	axial strain
ε_{yy}	transverse strain
ε_{xy}	shear strain
$\boldsymbol{\varepsilon}$	Green–Lagrange strain tensor
$\boldsymbol{\varepsilon}^c$	component of the Green–Lagrange strain tensor belongs to the centerline
$\boldsymbol{\varepsilon}^k$	component of the Green–Lagrange strain tensor belongs to higher-order terms
$\boldsymbol{\varepsilon}_v^c$	Voigt strain vector belonging to the centerline
$\boldsymbol{\varepsilon}_v^k$	Voigt strain vector belonging to higher-order terms
$\boldsymbol{\sigma}_v$	Voigt stress vector
k_s	shear correction factor
λ, μ	Lame's parameters
G	shear modulus
$\mathbf{D}^0$	modified matrix of elastic coefficient without Poisson's ratio
$\mathbf{D}^v$	matrix of elastic coefficient with Poisson's ratio
$\mathbf{T}$	transformation matrix
$\mathbf{Q}_{in}(\mathbf{e})$	internal elastic force vector
$\mathbf{q}_\mathrm{ext}$	constant directional vector for an external force
λ_ext	variable scalar loading parameter for an external force
$\mathbf{F}_\mathrm{ext}$	external force
Δl	arc-length constant for load estimation
$\Delta\mathbf{u}$	incremental displacement vector
U	strain energy
$\mathbf{K}_t$	tangent stiffness matrix
ε	error estimate
P	upper load limit
b	cross-section width of the frame
h	cross-section height of the frame
L	length of the one arm of the frame
E	Young's modulus
γ	Poisson's ratio

Acknowledgments: The authors gratefully acknowledge the Harbin Institute of Technology and China Scholarship Council (CSC) for providing an adequate environment for this research.

Funding information: This research was supported by the "Independent Research and Development project of State Key Laboratory of Green Building in Western China" (LSZZ202209).

Author contributions: All authors have accepted responsibility for the entire content of this manuscript and approved its submission.

Conflict of interest: Authors state no conflict of interest.

References

[1] Shabana AA. Definition of the slopes and the finite element absolute nodal coordinate formulation. Multibody Syst Dyn. 1997;1(3):339–48.
[2] Shabana AA. Definition of ANCF finite elements. J Comput Nonlinear Dyn. 2015;10(5):054506(1–5).
[3] Shabana AA. Computational continuum mechanics. 3rd ed. Hoboken (NJ), USA: John Wiley & Sons Ltd; 2018. p. 363.
[4] Shabana AA. ANCF tire assembly model for multibody system applications. J Comput Nonlinear Dyn. 2015;10(2):024504(1–4).
[5] Yu Z, Liu Y, Tinsley B, Shabana AA. Integration of geometry and analysis for vehicle system applications: Continuum-based leaf spring and tire assembly. J Comput Nonlinear Dyn. 2016;11(3):031011(1–11).
[6] Wang T, Tinsley B, Patel MD, Shabana AA. Nonlinear dynamic analysis of parabolic leaf springs using ANCF geometry and data acquisition. Nonlinear Dyn. 2018;93:2487–515. doi: 10.1007/s11071-018-4338-3.
[7] Cui Y, Lan P, Zhou H, Yu Z. The rigid-flexible-thermal coupled analysis for spacecraft carrying large-aperture paraboloid antenna. J Comput Nonlinear Dyn. 2020;15(3):031003(1–13).
[8] Liu C, Tian Q, Yan D, Hu H. Dynamic analysis of membrane systems undergoing overall motions, large deformations and wrinkles via

thin shell elements of ANCF. Comput Methods Appl Mech Eng. 2013;258:81–95. doi: 10.1016/j.cma.2013.02.006.
[9] Li K, Tian Q, Shi J, Liu D. Assembly dynamics of a large space modular satellite antenna. Mech Mach Theory. 2019;142(103601):1–18.
[10] Shabana AA, Eldeeb AE. Motion and shape control of soft robots and materials. Nonlinear Dyn. 2021;104:165–89. doi: 10.1007/s11071-021-06272-y.
[11] Huang X, Zou J, Gu G. Kinematic modeling and control of variable curvature soft continuum robots. IEEE/ASME Trans. Mechatronics. 2021;26:1–11.
[12] Hu H, Tian Q, Liu C. Computational dynamics of soft machines. Acta Mech Sin. 2017;33:516–28.
[13] Yoo W-S, Dmitrochenko O, Pogorelov DY. Review of finite elements using absolute nodal coordinates for large-deformation problems and matching physical experiments. ASME 2005 International design Engineering Technical Conferences and Computers and Information in Engineering Conference. 2005 Sep 24–28; Long Beach (CA), USA. ASME, 2005.
[14] Gerstmayr J, Hiroyuki S, Aki M. Review on the absolute nodal coordinate formulation for large deformation analysis of multibody systems. J Comput Nonlinear Dyn. 2013;8(3):031016(1–12).
[15] Dmitrochenko O, Mikkola A. Digital nomenclature code for topology and kinematics of finite elements based on the absolute nodal co-ordinate formulation. Proc Inst Mech Eng Part K J Multi-body Dyn. 2011;225(1):34–51.
[16] Luo K, Liu C, Tian Q, Hu H. Nonlinear static and dynamic analysis of hyper-elastic thin shells via the absolute nodal coordinate formulation. Nonlinear Dyn. 2016;85:949–71.
[17] Li J, Liu C, Hu H, Zhang S. Analysis of elasto-plastic thin-shell structures using layered plastic modeling and absolute nodal coordinate formulation. Nonlinear Dyn. 2021;105:2899–920.
[18] Nachbagauer K, Gerstmayr J. Structural and continuum mechanics approaches for a 3D shear deformable ANCF beam finite element: Application to buckling and nonlinear dynamic examples. J Comput Nonlinear Dyn. 2013;9(1):1–8. doi: 10.1115/1.4025282.
[19] Shaukat AR, Lan P, Wang J, Wang T. In-plane nonlinear postbuckling analysis of circular arches using absolute nodal coordinate formulation with arc-length method. Proc Inst Mech Eng Part K J Multi-body Dyn. 2021 Sep;235(3):297–311.
[20] Wang J, Wang T. Buckling analysis of beam structure with absolute nodal coordinate formulation. Proc Inst Mech Eng Part C J Mech Eng Sci. 2021 May;235(9):1585–92.
[21] Reis PM. A perspective on the revival of structural (In)stability with novel opportunities for function: From Buckliphobia to Buckliphilia. J Appl Mech. 2016;82(11):1–4.
[22] Cox BS, Groh RMJ, Avitabile D, Pirrera A. Exploring the design space of nonlinear shallow arches with generalised path-following. Finite Elem Anal Des. 2018;143:1–10.
[23] Hunt G, Champneys A, Dodwell T, Groh R, Neville R, Pirrera A, et al. Happy Catastrophe: recent progress in analysis and exploitation of elastic instability. Front Appl Math Stat. 2019;5:34.
[24] Pal A, Restrepo V, Goswami D, Martinez RV. Exploiting mechanical instabilities in soft robotics: Control, sensing, and actuation. Adv Mater. 2021;33(19):1–18.
[25] Shabana AA, Gantoi FM, Brown MA. Integration of finite element and multibody system algorithms for the analysis of human body motion. Procedia IUTAM. 2011;2:233–40.
[26] Orzechowski G, Fraczek J. Nearly incompressible nonlinear material models in the large deformation analysis of beams using ANCF. Nonlinear Dyn. 2015;82:451–64.
[27] Maqueda LG, Mohamed AA, Shabana AA. Use of General Nonlinear Material Models in Beam Problems: Application to Belts. J Comput Nonlinear Dyn. 2010;5:021003.
[28] Pil Jung S, Won Park T, Sun Chung W. Dynamic analysis of rubber-like material using absolute nodal coordinate formulation based on the non-linear constitutive law. Nonlinear Dyn. 2011;63:149–57.
[29] Karl-Eugen K. The history of the theory of structures – from arch analysis to computational mechanics. Berlin, Germany: Ernst & Sohn Verlag; 2008.
[30] Timoshenko SP, Gere JM. Theory of elastic stability. 17th ed. London, UK: McGraw; 1963. p. 541
[31] Koiter WT. Post-Buckling Analysis of a Simple Two-Bar Frame. Almquist and Wiksell Stockholm, Sweden: 1967. p. 337–54.
[32] Roorda J, Chilver AH. Frame buckling: An illustration of the perturbation technique. Int J Non Linear Mech. 1970;5(2):235–46.
[33] Lee S-L, Manuel FS, Rossow EC. Large deflections and stability of elastic frame. J Eng Mech Div. 1968;94(2):521–48.
[34] Akkoush EA, Toridis TG, Khozeimeh K, Huang HK. Bifurcation, pre- and post-buckling analysis of frame structures. Comput Struct. 1978;8(6):667–78.
[35] Simitses GJ, Giri J, Kounadis ANE. Nonlinear analysis of portal frames. Int J Numer Methods Eng. 1981;17:123–32.
[36] Simitses GJ, Giri J. Asymmetrically loaded portal frames. Comput Struct. 1984;19(4):555–8.
[37] Kounadis AN, Giri J, Simitses GJ. Nonlinear stability analysis of an eccentrically loaded two-bar frame. J Appl Mech Trans ASME. 1977;44(4):701–6.
[38] Pignataro M, Rizzi N. The effect of multiple buckling modes on the postbuckling behavior of plane elastic frames. Part I. Symmetric Frames. J Struct Mech. 1982;10(4):437–58.
[39] Rizzi N, Pignataro M. The effect of multiple buckling modes on the postbuckling behavior of plane elastic frames. Part II. Symmetric frames. J Struct Mech. 1982;10(4):459–74.
[40] Pignataro M, Rizzi N. On the interaction between local and overall buckling of an asymmetric portal frame. Meccanica. 1983;18(2):92–6.
[41] Pacoste C, Eriksson A. Beam elements in instability problems. Comput Methods Appl Mech Eng. 1997;144(1–2):163–97.
[42] Waszczyszyn Z, Janus-Michalska M. Numerical approach to the "exact" finite element analysis of in-plane finite displacements of framed structures. Comput Struct. 1998;69(4):525–35.
[43] Galvão AS, Gonçalves PB, Silveira RAM. Post-buckling behavior and imperfection sensitivity of L-frames. Int J Struct Stab Dyn. 2005;5(1):19–35.
[44] Basaglia C, Camotim D, Silvestre N. Post-buckling analysis of thin-walled steel frames using generalised beam theory (GBT). Thin-Walled Struct. 2013;62:229–42. doi: 10.1016/j.tws.2012.07.003.
[45] Yeong-Bin Y, Shyh-Rong K. Theory and analysis of nonlinear framed structures. 1st ed. Upper Saddle River (NJ), USA: Prentice Hall; 1994. p. 569.
[46] Yeong-Bin Y, Anquan C, Song H. Research on nonlinear, post-buckling and elasto-plastic analyses of framed structures and curved beams. Meccanica. 2020;56:1587–612. doi: 10.1007/s11012-020-01182-6.
[47] Omar MA, Shabana AA. A two-dimensional shear deformable beam for large rotation and deformation problems. J Sound Vib. 2001;243(3):565–76.
[48] Patel M, Shabana AA. Locking alleviation in the large displacement analysis of beam elements: the strain split method. Acta Mech. 2018;229:2923–46.

[49] Gerstmayr J, Matikainen MK, Mikkola AM. A geometrically exact beam element based on the absolute nodal coordinate formulation. Multibody Syst Dyn. 2008;20(4):359–84.
[50] Shen Z, Li P, Liu C, Hu G. A finite element beam model including cross-section distortion in the absolute nodal coordinate formulation. Nonlinear Dyn. 2014;77:1019–33.
[51] Orzechowski G, Shabana AA. Analysis of warping deformation modes using higher order ANCF beam element. J Sound Vib. 2016;363:428–45.
[52] Shabana AA, Mikkola AM. Use of the finite element absolute nodal coordinate formulation in modeling slope discontinuity. J Mech Des Trans ASME. 2003;125(2):342–50.
[53] Wempner GA. Discrete approximations related to nonlinear theories of solids. Int J Solids Struct. 1971;7(11):1581–99.
[54] Riks E. An incremental approach to the solution of snapping and buckling problems. Int J Solids Struct. 1978;15(7):529–51.
[55] Crisfield MA. A fast incremental/iterative solution procedure that handles "Snap-through". Comput Struct. 1981;13(1–3):55–62.
[56] de Borst R, Crisfield MA, Remmers JJC, Verhoosel CV. Non-linear finite element analysis of solids and structures. Chichester, UK: John Wiley & Sons; 2012.
[57] Simitses G, Hodges DH. Fundamentals of structural stability. 1st ed. Oxford, UK: Butterworth-Heinemann; 2006.